
Article:
Zhu, C. orcid.org/0000-0002-5516-661X, Hobbs, M.J., Grainger, M.P. et al. (1 more author) (2018) Design and realization of a wide field of view infrared scanning system with an integrated micro-electromechanical system mirror. Applied Optics, 57 (36). pp. 10449-10457. ISSN 0003-6935

https://doi.org/10.1364/AO.57.010449

Research Article Vol. 57, No. 36 / 20 December 2018 / Applied Optics 10449

applied optics

Design and realization of a wide field of view infrared scanning system with an integrated micro-electromechanical system mirror

Chengxi Zhu, Matthew J. Hobbs, Matthew P. Grainger, and Jon R. Willmott*

Electronic and Electrical Engineering Department, University of Sheffield, Western Bank, Sheffield, S10 2TN, UK
**Corresponding author: j.r.willmott@sheffield.ac.uk*

Received 14 August 2018; revised 1 October 2018; accepted 21 October 2018; posted 24 October 2018 (Doc. ID 342288); published 13 December 2018

We present a wide field of view (FOV) infrared scanning system, designed for single-pixel near-infrared thermal imaging. The scanning system consisted of a two-axis micro-electromechanical system (MEMS) mirror that was incorporated within the lens. The optical system consisted of two groups of lenses and a silicon avalanche photodiode. The system was designed for both the production of thermal images and also to utilize the techniques of radiation thermometry to measure the absolute temperature of targets from 500°C to 1100°C. Our system has the potential for real-time image acquisition, with improved data acquisition electronics. The FOV of our scanning system was ±30° when fully utilizing the MEMS mirror's scanning angle of ±5°. The pixel FOV (calculated from the distance to target size ratio) was 100:1. The image quality was analyzed, including the modulation transfer function, spot diagrams, ray fan plots, lateral chromatic aberrations, distortion, relative illumination, and size-of-source effect. The instrument was fabricated in our laboratory, and one of the thermal images, which was taken with the new lens, is presented as an example of the instrument optical performance.

https://doi.org/10.1364/AO.57.010449

1. INTRODUCTION

Temperature is an essential measurement in metrology that pervades our daily life. It represents the average kinetic energy of particles in an object, which can be linked to many physical and chemical phenomena. Radiation thermometry is a widely used noncontact temperature measurement technique, with fast response time and wide temperature measurement range, and it does not contaminate the measurand [1]. This technique has been applied in various fields, such as the metallurgical industry [2], additive manufacturing [3,4], and environmental monitoring [5]. When temperature measurements are undertaken, measurement uncertainty and traceability are key to measuring useful data [6]. To achieve this, instruments must have high responsivity, low noise, well-defined measurement area, and careful calibration [7]. The development of high-quality noncontact temperature measurement instruments focuses on engineering refinements in aspects such as optical, electronic, and system design, and this enables good thermal metrology.

Many novel instruments have been designed and realized within the field of noncontact temperature measurement [8]. One of these instruments is the radiation thermometer [9,10]. A typical radiation thermometer is composed of an on-axis optical system and a single-pixel detector (SPD). Due to the relatively simple structure, this type of instrument has many advantages, such as the well-defined measurement field and practicable calibration to SI units with low uncertainty. However, a radiation thermometer can only measure the temperature of one point on the measurand. If the thermal distribution of the whole measurand is required, the measurement must be repeated at different locations, and the data must be assembled into a map of the measured positions. Among the problems with this approach are that the thermal condition of a target may have changed during the finite time over which such a measurement takes place. Various factors introduce additional uncertainties, leading to the poor traceability for measuring the thermal distribution of a target.

Thermal cameras are becoming popular for use in noncontact temperature measurements, especially in thermal distribution measurements [9,10]. A typical thermal camera consists of an objective lens and a focal plane array (FPA) detector. The camera can produce high resolution thermal images of an object, directly benefiting from the large pixel count of a typical FPA detector [11]. However, this property also raises challenges to the design of a quantitative temperature measurement system, because of the nonuniformity of spectral responsivity and

cross talk among large numbers of pixels [12,13]. In particular, the existence of size-of-source effect (SSE) changes the instantaneous field of view (IFOV), which represents the measurement area due to each separate pixel. SSE describes the phenomenon that a pixel receives radiation from the region outside the nominal measurement area. This leads to an unpredictable and imprecise measurement across the target [14]. Thermal cameras cannot be used for accurate temperature measurements, unless they are calibrated and carefully characterized by highly skilled engineers, which leads to a significant concomitant increase in cost.

Single-pixel imaging systems, equipped with digital micromirror devices (DMDs), have been demonstrated in different approaches for producing thermal images [15,16]. One of the latest DMD-based systems can achieve 256 pixel × 256 pixel resolution at a frame rate of 11 Hz [17]. In these systems, DMDs perform as masks to pixelate the scene by micromirrors and choose the specified measurement area by pre-set DMD patterns. Different algorithms are adopted to reconstruct the image, which is one of the main advantages. In addition, these systems do not have the problem of the nonuniformity of spectral responsivity and cross talk due to use of an SPD. However, when a DMD-based imaging system is applied in absolute temperature measurements, the internal reflection among micromirrors and the window leads to an increased SSE for measurements. Meanwhile, the SSE of each pixelated measurement area is also determined by the DMD patterns while viewing the same scene. In this case, calibrations are required for each pixelated measurement area under various DMD patterns. Furthermore, the commercial DMD's window blocks the waveband above 2.5 μm (DLP2010NIR, Texas Instruments), which limits the temperature measurement range. In currently reported incarnations, we believe that DMD-based single-pixel imaging systems are not suitable for absolute temperature measurements, due to these challenges.

Considering the limitations of radiation thermometers, thermal cameras, and DMD-based single-pixel imaging systems, we found it necessary to develop a multipurpose instrument to map temperatures accurately, traceably, and quickly across an object. An infrared scanning imager, equipped with a two-axis scanning system and an SPD, would combine some of the advantages of both the radiation thermometer and thermal camera. Infrared scanning imagers can produce thermal images directly and measure absolute temperature accurately, while maintaining a relatively low cost. Galvo scanners and MEMS mirrors are two widely applied components in scanning instruments [18–20]. Compared to Galvo scanners, MEMS mirrors have properties of fast scanning speed and small package size, allowing them to be used in a portable instrument. Yet the mirror size is smaller than 5 mm in diameter, and the scanning angle is lower than ±5° for most commercial MEMS mirrors. To develop an infrared scanning imager, based on a MEMS mirror, challenges fall on the design of an optical scanning system if it is to make full use of the MEMS mirror size and scanning angle.

In this paper, we present a MEMS mirror-based infrared scanning system, equipped with a silicon (Si) avalanche photodiode (APD). Our instrument was designed for measuring temperatures from 500°C to 1100°C. The field of view (FOV) of our system was ±30°, the focal length was 18 mm, and the F-number was 16. The instrument was fabricated in our laboratory and used to produce thermal images of targets illuminated by an approximate blackbody furnace.

2. THEORETICAL ANALYSIS

The schematic design of our system consisted of two groups of lenses, a MEMS mirror (Mirrocle Technologies Inc.) and an Si APD, as shown in Fig. 1. Rays emitted from a measurand are collected by the first group, folded by the MEMS mirror, and focused by the second group onto the Si APD. The MEMS mirror was 5 mm in diameter, with a maximum scanning angle of ±5°. The Si APD active area was 0.2 mm in diameter. The FOV was ±30° by design. The system was to be used for imaging and, therefore, high optical resolution was required.

Distance-to-target-size ratio (D:S) (known as field of view in radiation thermometer terminology) allows the simple calculation of the area over which any particular radiation thermometer measures. It also quantifies the limit of an instrument's ability to distinguish the thermal features across an object. It is the ratio of the measurement distance to the measurement area upon the measurand, as shown in Eq. (1). It is one of the key parameters that characterizes a radiation thermometer. Radiation thermometers are often sensitive to small fractions of radiant power from considerable distances outside their fields of view, and so D:S must be measured for a fraction of the total power. The fraction of enclosed radiant power, by percent (α), was defined for our optical system as 90%, giving a D:S of 100:1; which is typical for an industrial radiation thermometer [21]. This led us to a focal length for the system of 18 mm:

$$D{:}S = f'/(\alpha D_p), \tag{1}$$

where f' is the focal length, α is the fraction of enclosed radiant power percent of the measurement area, and D_p is the diameter of the APD active area.

Signal-to-noise ratio (SNR) is an important parameter for noncontact temperature measurement, which increases with

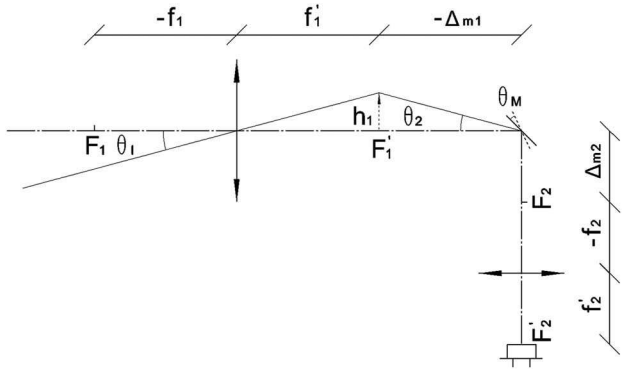

Fig. 1. Schematic diagram of our optical system. f_1 is the focal length of the first group of lenses; f_2 is the focal length of the second group of lenses; h_1 is the intermediate image height; Δ_{m1} is the distance between the MEMS mirror center to the first focal point in image space; Δ_{m2} is the distance between the MEMS mirror center to the second focal point in object space; θ_1 is the incident angle of the chief ray at maximum FOV; θ_2 is the incident angle of the chief ray to the MEMS mirror; and θ_M is the half-maximum scanning angle of the MEMS mirror.

measurand temperature and ultimately limits the minimum resolvable temperature [22]. A maximized numerical aperture (low F-number), within design constraints, is desirable so that the system receives a maximum of radiant power from the measurand, achieving the highest SNR for any given measurand temperature. The F-number is determined by the smallest optical element, which is the MEMS mirror in our design. The problem posed during our system design process focused on designing a scanning system, with the lowest F-number, while meeting the requirements of FOV and D:S. The F-number of the system can be expressed as

$$F\text{-number} = \frac{f'}{(f_1'/\Delta_{m1}) \times (D_{\mathrm{MEMS}} \times \cos 45°)}, \tag{2}$$

where D_{MEMS} is the dimension of the MEMS mirror.

The relationship between the effective focal length of a system and each group of lenses can be expressed as

$$f' = \frac{f_1' f_2'}{\Delta_{m1} + \Delta_{m2}}. \tag{3}$$

Figure 2 shows the relationship between F-number, f_1', and Δ_{m1} with the consideration of initial conditions of the system, listed from Eqs. (4)–(6). The smallest F-number of our system is 16.67 under the paraxial approximation. The system, with this F-number, is practicable for high temperature measurements, when used with the high sensitivity Si APD [23]. To achieve this F-number, f_1' and D_{MEMS} should be selected along the lowest blue edge in the diagram. When the focal length of the first group tends to infinity, the system becomes the combination of a telescope and an objective, which can be adopted as the initial structure for further optimization:

$$f' = 18 \text{ mm}, \tag{4}$$

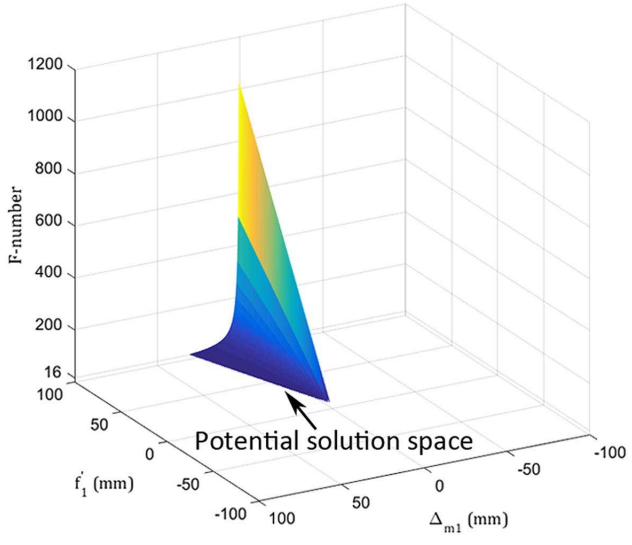

Fig. 2. Relationship between F-number, f_1', and Δ_{m1}. The diagram shows the potential solutions of F-number with various f_1' and Δ_{m1} (within ± 100 mm range). The blue area represents the system with a relatively small F-number, while the yellow area represents the system with a large F-number.

$$D_{\mathrm{MEMS}} = 5 \text{ mm}, \tag{5}$$

$$\theta_M \le 5°. \tag{6}$$

3. SYSTEM DESIGN

We were required to develop a two-dimensional scanning system, capable of measuring temperature over the range 500°C to 1100°C, across the optical waveband from 0.85 to 1.05 μm. The first-order design specifications of the optical system are shown in Table 1. The design wavelengths were selected as 0.85, 0.95, and 1.05 μm to match the spectral responsivity of the Si APD. The spatial frequency was determined to be 18 cycles per millimeter, due to the Si APD active area. The incident angle of the chief ray at the MEMS mirror surface was set to 10°, to make use of its full scanning angle of ±5°. The distance between the mirror and each adjacent element was arranged to be larger than 15 mm, to avoid mechanical interference between those components.

The design flow of this system was different from a typical lens design, as shown in Fig. 3. First, the system was optimized from the initial structure, derived from the aforementioned combination of a telescope and a converging lens. The MEMS mirror was replaced by a virtual intermediate plane. Second, the system was reversed, and the virtual plane was changed to the MEMS mirror. The system was then, once again, optimized under the multiconfiguration mode. Five configurations were set to 0, ±0.707, ±1.00 of FOV, associated with the scanning angle of the MEMS mirror, respectively. Finally, tolerances were analyzed to elucidate the expected system performance, following manufacturing and assembly. Once the system met the requirements at all phases, the design was regarded as ready for fabrication.

The data of the system are shown in Table 2. The schematic cross-section view is shown in Fig. 4. The system was composed of two lens groups, with five elements. The first group ranged from the first surface to the sixth surface. The second group ranged from the ninth surface to the 12th surface. The seventh surface was the reflecting surface of the MEMS mirror. The eighth surface was the stop aperture of the lens system. The first group would, alone, perform as a telescope, and in our system is transformed into a converging lens, to balance aberrations under the wide field of view.

4. RESULTS AND DISCUSSION

The image quality was analyzed for our lens system: it included the MTF diagram, spot diagrams, ray fan plots, lateral

Table 1. First-Order Specifications of the System

Item	Specification
Field of view	±30°
Focal length	18 mm
F-number	16.67
MEMS mirror scanning angle	±5°
Total system length	<150 mm
Clear aperture	<30 mm
Wavelength	0.85 to 1.05 μm

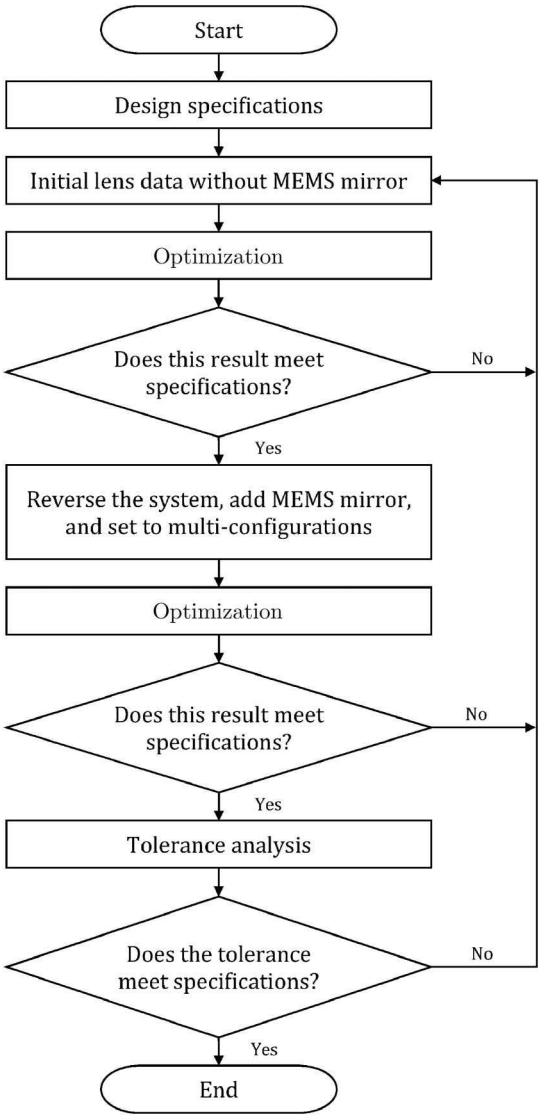

Fig. 3. Flow chart of the scanning system design.

Table 2. Data of the System

Surface Number	Radius of Curvature (mm)	Surface Separation (mm)	Glass	Semi-Diameter (mm)
1	160.000	3.000	N-LAK9	12.0
2	13.835	25.000		9.0
3	−18.313	4.000	N-SF11	8.0
4	−17.986	25.000		10.0
5	518.418	4.000	N-BAK4	7.5
6	−42.641	21.257		7.5
7	infinity	24.823	MEMS mirror	2.5
8	infinity	3.000	aperture	1.6
9	9.353	3.000	N-BAK4	5.0
10	25.530	12.000		3.5
11	−5.605	3.000	N-SF11	3.5
12	−13.200	13.766		5.0
13	infinity	-	image plane	0.1

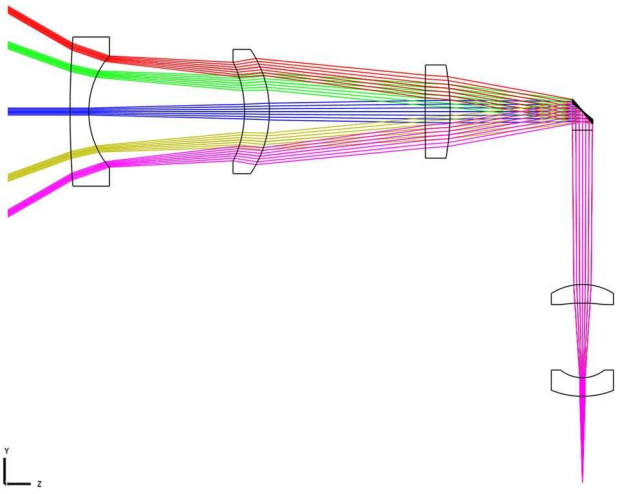

Fig. 4. Schematic cross-section view of the system.

chromatic aberration, distortion, relative illumination, and SSE. Among these analyses, distortion was studied to understand the relationship between FOV and scanning angle of the MEMS mirror. Relative illumination was undertaken to reveal the radiant power throughput variation from the center of the image to its corner. SSE was simulated to estimate the measurement area on a target.

The tolerance sensitivity of the system was analyzed before manufacturing. In practice, the image quality of an optical system usually changes after the fabrication, due to manufacturing and assembly errors. These errors mainly arise from three sources: surface deviations, positional changes, and material variations. If lenses are sensitive to these errors, manufacturing tolerances should be specified to a tighter level, leading to increased total cost. If the required tolerances are tighter than is practicable, given the available machine precision, the lens design is impractical and should be optimized again.

The lenses of our system were manufactured and antireflection-coated. The entire infrared scanning system was integrated at this phase, including the work of assembling and aligning. This was followed by a laboratory test phase.

A. Image Quality

Figure 5 shows the MTF diagram of the system for FOV of 0°, 20°, and 30°. The spatial frequency was set at 18 cycles per millimeter. The diffraction limit is shown as a solid black line. The tangential MTF curves are drawn in solid lines, while the sagittal curves are drawn in dashed lines. The minimum MTF is 0.5010, for a FOV of 30° in the sagittal direction. The MTF values for other FOVs are all larger than 0.5610.

Figure 6 shows the spot diagrams of the system, on the image (detector) surface. The scale bar of the diagram is 100 μm × 100 μm. The Airy disk is drawn as a solid circle in each graph. The RMS radii for FOV of 0°, 20°, and 30° are 11.074, 7.877, and 10.875 μm, respectively. The geometric (GEO) spot radii are 22.723, 20.417, and 24.893 μm, respectively. All spots are similar in extent to the Airy disk, which is 16.52 μm in radius.

Figure 7 shows the ray fan plots of the system for FOV of 0°, 20°, and 30°. The horizontal axis represents the relative

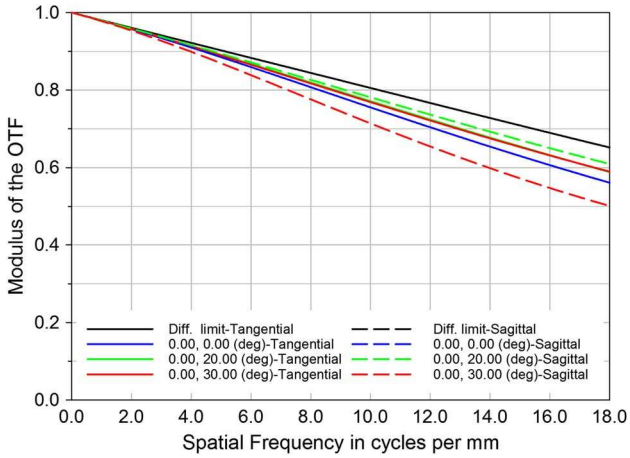

Fig. 5. MTF diagram of the system. The working distance was set to infinity.

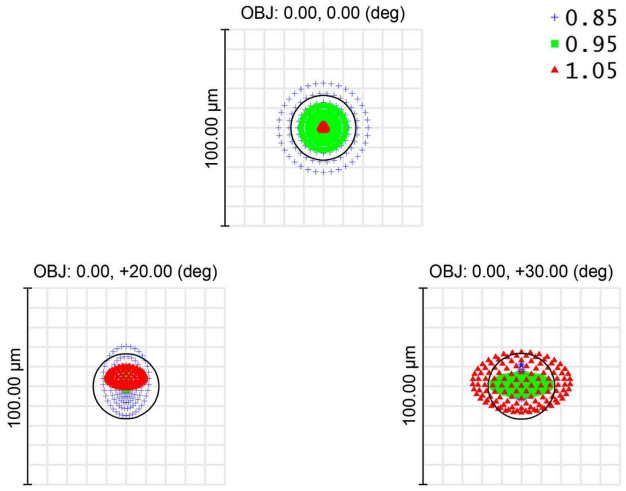

Fig. 6. Spot diagrams of the system. The working distance was set to infinity.

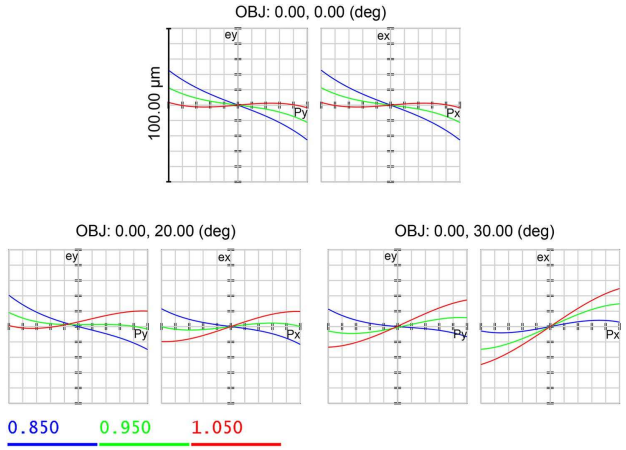

Fig. 7. Ray fan plots of the system. The working distance was set to infinity.

pupil height, and the vertical axis represents the transverse ray aberrations. The scale bar of the plot is 100 μm × 100 μm. The meridional ray aberration plot is shown at left, while the sagittal ray aberration plot is shown at right. Slight chromatic spherical aberrations and astigmatisms can be observed in these plots. Aberrations, in general, are less than 30 μm for each FOV.

Figure 8 shows the lateral chromatic aberration of the system. The middle wavelength (0.95 μm) was selected as the reference that is drawn in the green curve. The short wavelength (0.85 μm) is drawn in blue, and the long (1.05 μm) wavelength is drawn in red. The largest lateral chromatic aberration occurs at the maximum FOV for both short and long wavelengths, which are represented by the value of 13.879 and 14.783 μm, respectively.

Figure 9 shows the optical distortion of the system, where the horizontal axis represents the distortion, and the vertical axis represents the FOV from 0° to 30°. For this system, the distortion is defined by the base of the scanning angle of the MEMS mirror, as shown in Eq. (7). The maximum value is 1.73%, which occurs at the FOV of 18°. Previous research

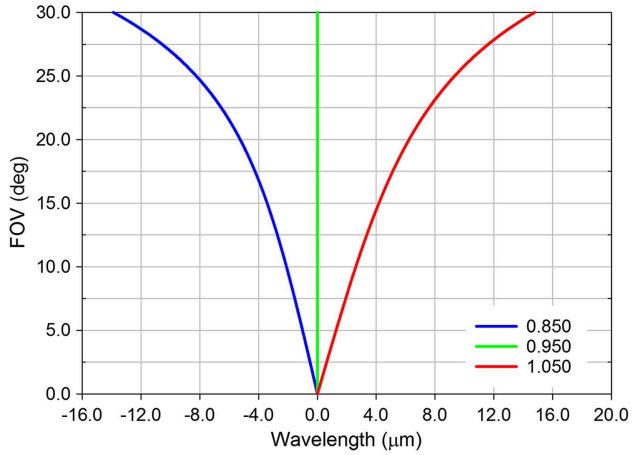

Fig. 8. Lateral chromatic aberration of the system. The working distance was set to infinity.

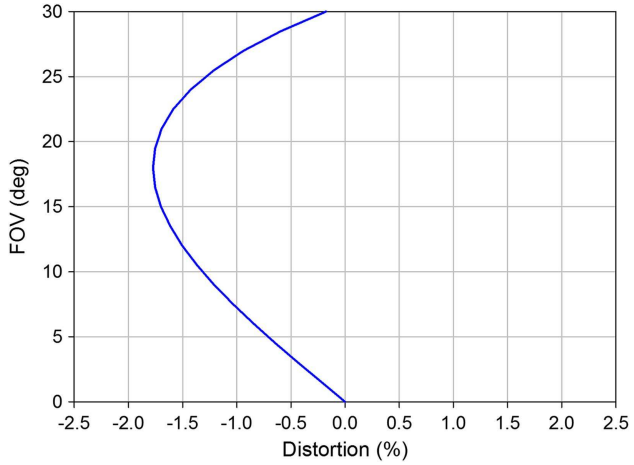

Fig. 9. Optical distortion of the system. The working distance was set to infinity.

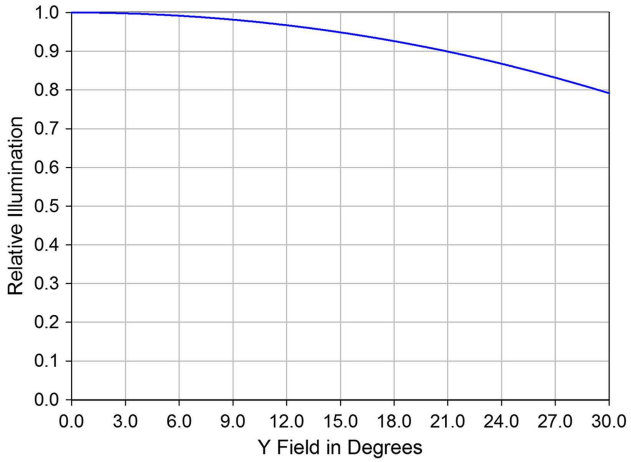

Fig. 10. Relative illumination of the system. The working distance was set to infinity.

indicated that the scanning angle of a MEMS mirror was not linear and was dependent upon the scanning speed and bias voltage [24]. Considering these factors, the system must be correctly calibrated for the combined distortion, with consideration of both the MEMS mirror nonlinearity and optical distortion:

$$\text{Distortion} = \left| \frac{\text{FOV}_{\text{actl}} - \text{FOV}_{\text{noml}}}{\text{HFOV}} \right|, \tag{7}$$

where FOV_{actl} is the actual FOV at each scanning step, FOV_{noml} is the nominal FOV at each scanning step, and HFOV is the half-field of view.

Figure 10 shows the relative illumination of the system, where the horizontal axis represents the FOV from 0° to 30°, and the vertical axis represents the relative illumination (%). The relative illumination decreases to 79.2% for FOV of 30°. The decrease will cause nonuniformity in the signal intensity across the image and introduce uncertainties within the measurements. The nonuniformity can be reduced to an acceptable level, with careful calibration and correction, under the full FOV, following instrument fabrication.

Figure 11 shows the simulated SSE, by Zemax OpticStudio, for the FOV of 0° and 30°, based on the direct measurement method [14]. Starting from our design in Fig. 4, the Si APD was replaced with a circular light source of 0.2 mm in diameter. The working distance was set to 5 m. The image quality, at this position, can be regarded as being very close to that which would be observed at infinity. Figure 11(a) shows the simulated energy of the measurement area across the Y direction, upon the target. Figure 11(b) shows that the measurement area is smaller than 51 mm in diameter, for an FOV of 0° and 30°. The D:S is around 98:1, which conforms to the design.

B. Tolerance Analysis

In this work, tolerance analysis was performed by Zemax OpticStudio, in sensitivity mode. A test wavelength of 0.95 μm was selected. The analysis was performed by the Monte Carlo method, with 100 simulations, under criteria of the RMS spot size and average diffraction MTF. Table 3

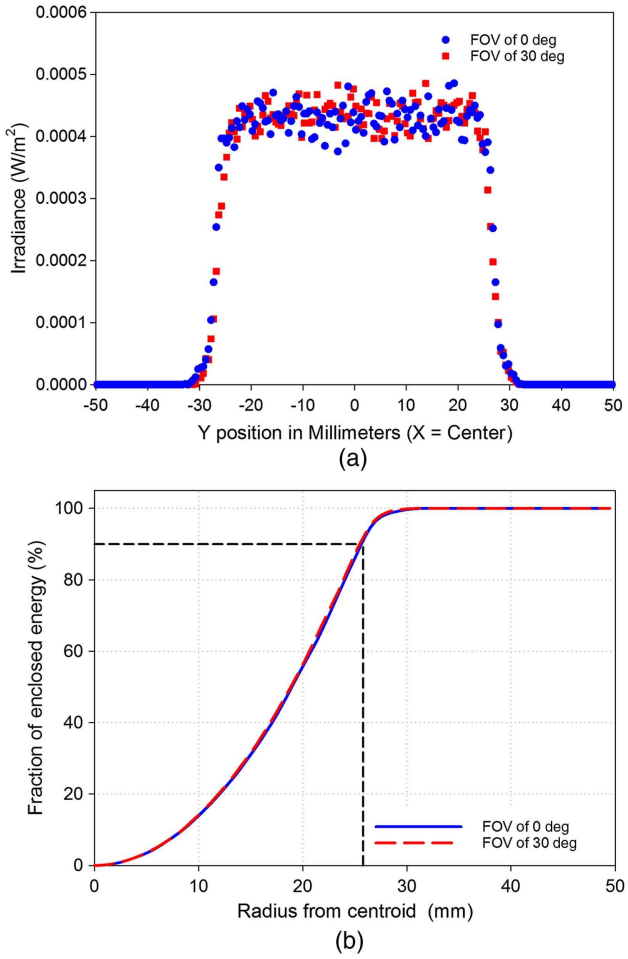

Fig. 11. Analysis of measurement areas on the target. (a) Measurement area extents are shown for FOV of 0° and 30°; (b) SSE is shown for FOV of 0° and 30°. The working distance was set to 5 m. The total input power was 1 W.

lists the detailed range of tolerance parameters. The MEMS mirror was offered as an off-the-shelf item, without the possibility of re-engineering it for our application. Its curvature radius tolerance was assumed to be 0, while the surface irregularity tolerance was assumed to be ±0.5 fringes. The remaining lenses were assumed with both curvature radius deviation and surface irregularity. All tolerances were specified, based on the achievable machine precision, according to manufacturing experience.

Table 4 shows the results of tolerance analysis for FOVs of 0°, 20°, and 30° at 0.95 μm. The standard deviation (SD) of each subject, computed 100 times, ranges from 0.001 to 0.032. The deviation between the mean and the design RMS spot size ranges from 2.74% (at FOV of 30°) to 10.63% (at FOV of 20°). The decrease between the mean and the design value of average MTF at 18 cycles per millimeter ranged from 0.52% (at FOV of 0°) to 3.56% (at FOV of 20°).

Figure 12 shows the RMS spot diagrams for all wavelengths under the worst condition found by the Monte Carlo simulation. The RMS spot size for FOV of 0°, 20°, and 30° are 17.142, 13.547, and 17.366 μm, respectively. Figure 13 shows

Table 3. Tolerance Parameter Ranges (at 0.95 μm)

Item	Specification
Radii of curvature of surfaces (fringes)	±4.0
Irregularity of lens surfaces (fringes)	±1.0
Irregularity of MEMS mirror surface (fringes)	±0.5
Center thickness (mm)	±0.1
Decentration X of surfaces (mm)	±0.02
Decentration Y of surfaces (mm)	±0.02
Tilt X of surfaces (degree)	±0.02
Tilt Y of surfaces (degree)	±0.02
Decentration X of elements (mm)	±0.02
Decentration Y of elements (mm)	±0.02
Tilt X of elements (degree)	±0.02
Tilt Y of elements (degree)	±0.02
Refractive index	±0.001
Abbe number (%)	±1.0

the MTF diagrams for all wavelengths under the worst condition. The minimum MTF value is 0.4114 for FOV of 30° in the tangential direction. We found that our fabricated system achieved performance which was, on average, close to the design specification. The tolerance analysis shows that even under the worst condition, which will occur with a very low probability, the system maintains good image quality.

C. Instrumentation Realization

Figure 14 shows the cross-section diagram of the instrument. Two groups of lenses were fixed in the lens housing beside the MEMS mirror, which was screwed onto a bracket. The Si APD was mounted on a three-dimension translation stage (not drawn in the diagram). All metal parts were made from aluminum alloy and anodized in black. All optical elements, including the MEMS mirror window, were coated with antireflection coating, effective from 0.85 to 1.05 μm. The MEMS mirror was adjusted to match its center to the optical axis. Although the instrument was designed with an infinity working distance, it could be focused more closely by changing the distance between the lens and the APD.

Figure 15 shows a photograph of the lens assembly, when used to thermally image a test object measurand. The measurand was an "*s*" shape slot cut from a stainless steel sheet. The dimension of the "*s*" shape was 26 mm × 18 mm. The width of the slot was approximately 2 mm. The measurand was illuminated by a furnace, which was set to 1000°C. The working distance was 300 mm.

Figure 16 shows a 160 pixel × 120 pixel thermal image of the measurand. The image was taken within 8 s, with the integration time of each pixel being 400 μs. The frame rate is currently limited by the readout electronics. A higher frame rate could be expected with improvement in the readout electronics to enable an integration time per pixel of <10 μs, to ensure the instrument can fully use the speed of the MEMS mirror and Si APD [25,26]. The temperature bar scale spanned from blue (600°C) to red (1000°C). The temperature information of each effective pixel could be retrieved from the matrix that was used to form the diagram. The measurement uncertainty of our system can achieve ±1.8°C when imaging an object at 1000°C [27].

Our lens system successfully produced thermal images by means of scanning the FOV of an Si APD across a scene. In this way, we have achieved the aim of enabling the techniques of radiation thermometry to be used to produce two-dimensional thermal images.

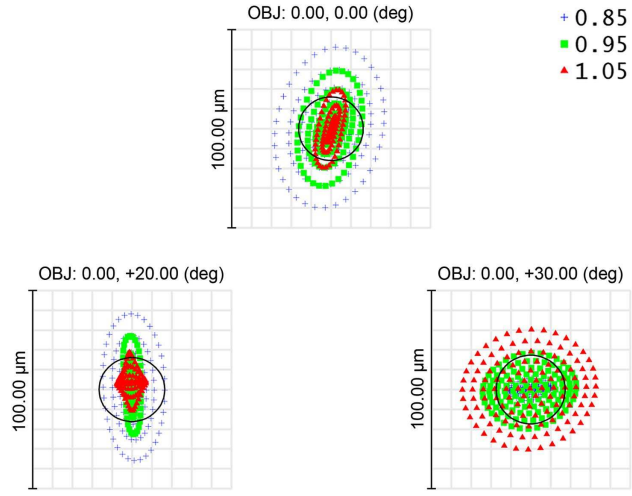

Fig. 12. Matrix of spot diagrams under the worst condition found during tolerance simulations. The working distance was set to infinity.

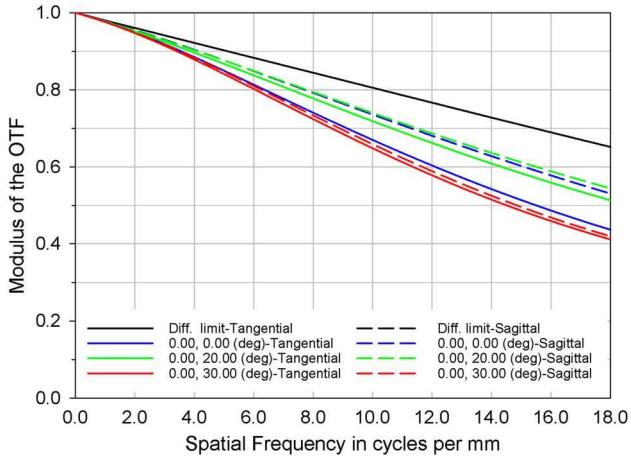

Fig. 13. MTF diagram under the worst condition found during tolerance simulations. The working distance was set to infinity.

Table 4. Tolerance Analysis (at 0.95 μm)

	RMS Spot Size (μm)			Average MTF (at 18 cycles per mm)		
FOV (deg)	Design	Mean/(SD)	Worst	Design	Mean/(SD)	Worst
0	9.347	9.650/(0.002)	14.743	0.5754	0.5724/(0.023)	0.4919
20	6.897	7.630(0.001)	11.354	0.6035	0.5820/(0.016)	0.5360
30	10.854	11.151(0.002)	16.118	0.5375	0.5327/(0.032)	0.4232

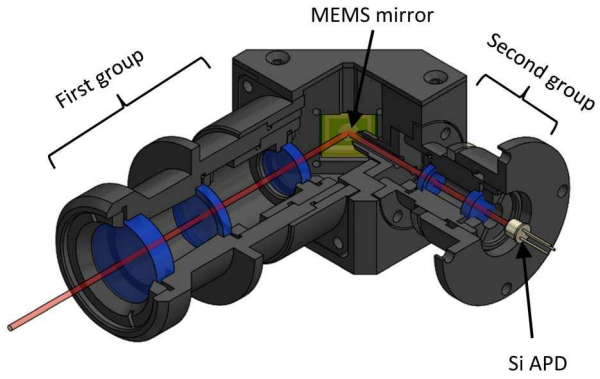

Fig. 14. Cross-section diagram of our lens. The red line indicates the optical axis.

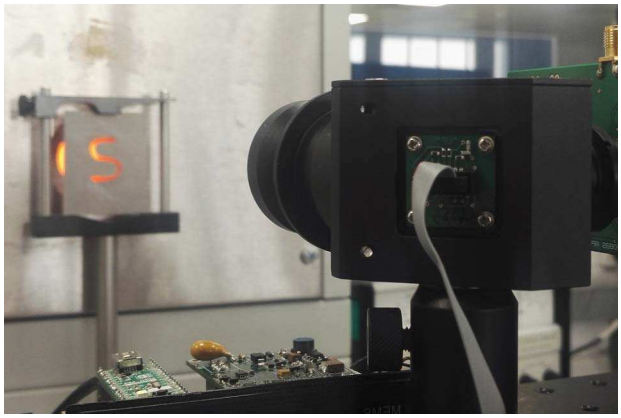

Fig. 15. Photograph of our lens system when used to thermally image an approximate blackbody furnace. The working distance was 300 mm. The target was illuminated by a furnace set to 1000°C.

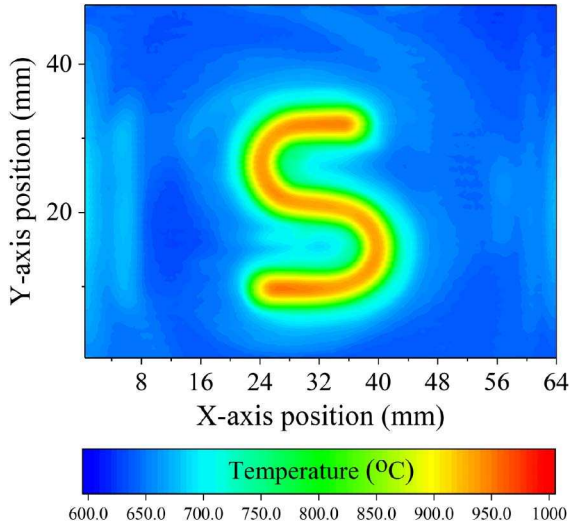

Fig. 16. Thermal image of the measurand, chosen as a visual illustration of the performance of our lens system.

5. CONCLUSION

We have presented the design and realization of an infrared scanning system with an integrated MEMS mirror. To the best of our knowledge, it is the first MEMS-based scanning system that can be used for both thermal images and to measure the absolute temperature of a target; from 500°C to 1100°C, at the wavelength from 0.85 to 1.05 μm. Our system has the potential for real-time image acquisition, with improved data acquisition electronics. The optical system was designed to fully utilize the 5 mm diameter mirror and its ±5° scanning angle. The FOV of the instrument achieved ±30°. The pixel FOV was 100:1. The lens system is suitable to be used for a wide range of high temperature or near-infrared sensing applications.

Funding. Engineering and Physical Sciences Research Council (EPSRC) (EP/M009106/1).

REFERENCES

1. J. R. Howell and R. Siegel, *Thermal Radiation Heat Transfer* (Hemisphere, 1992).
2. R. Usamentiaga, J. Molleda, D. F. Garcia, J. C. Granda, and J. L. Rendueles, "Temperature measurement of molten pig iron with slag characterization and detection using infrared computer vision," IEEE Trans. Instrum. Meas. **61**, 1149–1159 (2012).
3. E. Rodriguez, J. Mireles, C. A. Terrazas, D. Espalin, M. A. Perez, and R. B. Wicker, "Approximation of absolute surface temperature measurements of powder bed fusion additive manufacturing technology using in situ infrared thermography," Addit. Manuf. **5**, 31–39 (2015).
4. M. Zavala-Arredondo, N. Boone, J. Willmott, D. T. D. Childs, P. Ivanov, K. M. Groom, and K. Mumtaz, "Laser diode area melting for high speed additive manufacturing of metallic components," Mater. Des. **117**, 305–315 (2017).
5. T. Lopez, H. E. Thomas, A. J. Prata, A. Amigo, D. Fee, and D. Moriano, "Volcanic plume characteristics determined using an infrared imaging camera," J. Volcanol. Geotherm. Res. **300**, 148–166 (2015).
6. P. R. N. Childs, J. R. Greenwood, and C. A. Long, "Review of temperature measurement," Rev. Sci. Instrum. **71**, 2959–2978 (2000).
7. P. Saunders, *Radiation Thermometry: Fundamentals and Applications in the Petrochemical Industry* (SPIE, 2007).
8. J. Dixon, "Radiation thermometry," J. Phys. E **21**, 425–436 (1988).
9. A. Rogalski, "Infrared detectors: status and trends," Prog. Quantum Electron. **27**, 59–210 (2003).
10. Z. M. Zhang, B. K. Tsai, and G. Machin, *Radiometric Temperature Measurements: II. Applications* (Academic, 2009).
11. F. Blais, "Review of 20 years of range sensor development," J. Electron. Imaging **13**, 231 (2004).
12. J. G. Harris and Y.-M. Chiang, "Nonuniformity correction of infrared image sequences using the constant-statistics constraint," IEEE Trans. Image Process. **8**, 1148–1151 (1999).
13. M. A. Itzler, R. D. Younger, J. C. Campbell, K. A. McIntosh, J. W. Chludzinski, D. C. Oakley, L. J. Mahoney, J. E. Funk, J. P. Donnelly, and S. Verghese, "Crosstalk analysis of integrated Geiger-mode avalanche photodiode focal plane arrays," in *Advanced Photon Counting Techniques III* (Society of Photo-optical Instrumentation Engineers, 2009), p. 73200Q.
14. H. W. Yoon, D. W. Allen, and R. D. Saunders, "Methods to reduce the size-of-source effect in radiometers," Metrologia **42**, 89–96 (2005).
15. M. F. Duarte, M. A. Davenport, D. Takhar, J. N. Laska, T. Sun, K. F. Kelly, and R. G. Baraniuk, "Single-pixel imaging via compressive sampling," IEEE Signal Process. Mag. **25**, 83–91 (2008).
16. M. P. Edgar, G. M. Gibson, R. W. Bowman, B. Sun, N. Radwell, K. J. Mitchell, S. S. Welsh, and M. J. Padgett, "Simultaneous real-time visible and infrared video with single-pixel detectors," Sci. Rep. **5**, 10669 (2015).

17. K. M. Czajkowski, A. Pastuszczak, and R. Kotynski, "Real-time single-pixel video imaging with Fourier domain regularization," Opt. Express **26**, 20009–20022 (2018).
18. N. Pelin Ayerden, U. Aygun, S. T. Holmstrom, S. Olcer, B. Can, J. L. Stehle, and H. Urey, "High-speed broadband FTIR system using MEMS," Appl. Opt. **53**, 7267–7272 (2014).
19. X. Lee and C. Wang, "Optical design for uniform scanning in MEMS-based 3D imaging lidar," Appl. Opt. **54**, 2219–2223 (2015).
20. A. Cogliati, C. Canavesi, A. Hayes, P. Tankam, V. F. Duma, A. Santhanam, K. P. Thompson, and J. P. Rolland, "MEMS-based hand-held scanning probe with pre-shaped input signals for distortion-free images in Gabor-domain optical coherence microscopy," Opt. Express **24**, 13365–13374 (2016).
21. Land Instruments International, "SPOT high precision pyrometers," https://www.ametek-land.com/-/media/ametekландinstruments/documentation/products/fixedspotnoncontactthermometers/spot/ametek_land_spot_brochure_marcom0355_rev_15.pdf.
22. M. Vollmer and K.-P. Möllmann, *Infrared Thermal Imaging: Fundamentals, Research and Applications* (Wiley, 2017).
23. M. J. Hobbs, M. P. Grainger, C. Zhu, C. H. Tan, and J. R. Willmott, "Quantitative thermal imaging using single-pixel Si APD and MEMS mirror," Opt. Express **26**, 3188–3198 (2018).
24. V. Milanovic, "Linearized gimbal-less two-axis MEMS mirrors," in *Optical Fiber Communication Conference* (2009), p. JThA19.
25. C. L. Hoy, N. J. Durr, and A. Ben-Yakar, "Fast-updating and nonrepeating Lissajous image reconstruction method for capturing increased dynamic information," Appl. Opt. **50**, 2376–2382 (2011).
26. S. Z. Sullivan, R. D. Muir, J. A. Newman, M. S. Carlsen, S. Sreehari, C. Doerge, N. J. Begue, R. M. Everly, C. A. Bouman, and G. J. Simpson, "High frame-rate multichannel beam-scanning microscopy based on Lissajous trajectories," Opt. Express **22**, 24224–24234 (2014).
27. M. J. Hobbs, C. Zhu, M. P. Grainger, C. H. Tan, and J. R. Willmott, "Quantitative traceable temperature measurement using novel thermal imaging camera," Opt. Express **26**, 24904–24916 (2018).